

Decomposition of the spin- $\frac{1}{2}$ Heisenberg chain compound Sr_2CuO_3 in air and water: An EPR and magnetic susceptibility study of $\text{Sr}_2\text{Cu}(\text{OH})_6$

J. M. Hill, D. C. Johnston, and L. L. Miller

Ames Laboratory and Department of Physics and Astronomy, Iowa State University, Ames, Iowa 50011

(Dated: February 1, 2008)

The reaction of Sr_2CuO_3 with air and liquid water was studied to address the origin of the reported variable Curie-Weiss impurity contribution to the magnetic susceptibility χ of this compound at low temperatures. Sr_2CuO_3 was found to decompose upon exposure to either of these environments. The compound $\text{Sr}_2\text{Cu}(\text{OH})_6$ was identified as the primary reaction product. A pure sample of $\text{Sr}_2\text{Cu}(\text{OH})_6$ was then prepared separately. Electron paramagnetic resonance (EPR), isothermal magnetization versus magnetic field $M(H)$ and χ versus temperature T measurements demonstrate that $\text{Sr}_2\text{Cu}(\text{OH})_6$ contains weakly interacting Cu^{+2} magnetic moments with spin $S = \frac{1}{2}$ and average g -factor 2.133. From a fit of $\chi(T)$ by the Curie-Weiss law and of the $M(H)$ isotherms by modified Brillouin functions, the exchange interaction between adjacent Cu^{+2} spins was found to be $J/k_B = -1.06(4)$ K, a weakly antiferromagnetic interaction. Our results indicate that the previously reported, strongly sample-dependent, Curie-Weiss contribution to $\chi(T)$ of a polycrystalline Sr_2CuO_3 sample most likely arises from exposing the sample to air, resulting in a variable amount of paramagnetic $\text{Sr}_2\text{Cu}(\text{OH})_6$ on the surface of the sample.

PACS numbers: 75.20.Ck, 81.40.Rs, 76.30.Fc

I. INTRODUCTION

The physics of low-dimensional quantum spin systems has been intensively studied over the past decade due to its relevance to the physics of the layered cuprate superconductors and to the variety of unconventional magnetic and electronic properties exhibited by such materials. The field of low-dimensional quantum magnetism has a long history dating back to the early 1930s with the publication of the Bethe ansatz equations¹ from which in principle the eigenvalues of the spin $S = \frac{1}{2}$ Heisenberg chain can be obtained. By the early 1990s, research on spin-chain and spin-ladder materials related to the high-temperature superconductors had become a subfield of condensed matter physics. The current experimental work on spin-ladders has been driven by theory but is limited by the lack of known spin-ladder compounds, particularly metals. Of the cuprates, only $(\text{Sr,Ca})_{14}\text{Cu}_{24}\text{O}_{41}$ is known to become metallic and superconducting, and then only under high pressure.^{2,3} However, the interpretation of its properties is complicated by the fact that it is comprised of both Cu_2O_3 ladder and CuO_2 chain layers. To isolate the physics associated with one or the other type of spin configuration, it is desirable to study metallic compounds with either chains or ladders, but not both. For reviews of oxide spin-ladder and spin-chain compounds see Refs. 4,5,6,7.

Sr_2CuO_3 is a model spin- $\frac{1}{2}$ linear chain compound. It has an orthorhombic structure (space group Immm, Ref. 8) containing Cu^{+2} spins $S = \frac{1}{2}$. The orthorhombic structure is derived from the layered tetragonal K_2NiF_4 structure by removing lines of oxygen atoms parallel to the b axis from within the CuO_2 layers of the hypothetical tetragonal K_2NiF_4 -type compound Sr_2CuO_4 . Magnetic susceptibility studies^{9,10,11,12} show this compound to be a nearly ideal one-dimensional (1D) spin- $\frac{1}{2}$ Heisen-

berg antiferromagnet with a strong intrachain Cu-Cu exchange coupling $J/k_B = 2200 \pm 200$ K, while optical measurements^{13,14} yield $J/k_B = 2800\text{--}3000$ K. On the other hand, theoretical calculations¹⁵ indicate that J/k_B can be no larger than about 2300 K in this compound. Muon spin rotation/relaxation (μSR) and neutron diffraction measurements on single crystals^{16,17,18} revealed long-range antiferromagnetic ordering in this compound with a Néel temperature $T_N \simeq 5$ K and an ordered magnetic moment of $\approx 0.06 \mu_B/\text{Cu}$ atom. For the 1D Heisenberg model, logarithmic terms in the field theory expression for the magnetic susceptibility at very low temperatures yield an infinite slope as T approaches its finite value at 0 K.^{4,19,20} Takigawa *et al.* (Refs. 21,22,23) claim to have seen this behavior in their NMR data: a downturn with decreasing T was observed in the magnetic susceptibility at low T , but the downturn was not fitted well by the predicted logarithmic behavior. Theory also predicts separated spin and charge excitations near the Fermi energy called “spinon” and “holon” excitations, respectively, for 1D correlated systems (see for example Ref. 24). Angle-resolved photoemission spectroscopy (ARPES) measurements by Fujisawa *et al.* (Ref. 24) along the chains (b axis) show good qualitative agreement with these theoretical predictions. They observe two separate dispersions in the Brillouin zone, one which is reflected about kb/π (holon) and one which is not (spinon). However, quantitatively their measurements are not fitted well by theory.

A superconducting tetragonal phase, $\text{Sr}_2\text{CuO}_{3+\delta}$, has been reported to form under high pressure and to exhibit a superconducting transition temperature $T_c \approx 70$ K.^{25,26,27,28} However, the samples contained low superconducting volume fractions and showed semiconducting behavior above T_c rather than metallic behavior. Several groups^{29,30,31,32} subsequently reported high

pressure synthesis of nonsuperconducting samples and Kawashima *et al.* (Ref. 31) suggested that the superconductivity arose from $\text{Sr}_2\text{CaCu}_2\text{O}_y$ impurities. Tetragonal $\text{Sr}_2\text{CuO}_{3+\delta}$ can also be synthesized at ambient pressure^{33,34,35} and those samples were all also nonsuperconducting. The available evidence indicates that the oxygen content in this compound is variable;^{25,28,32,33,36} δ ranges from 0.08 to 0.9. Neutron diffraction measurements carried out on a superconducting and on a non-superconducting sample^{32,36} found no major differences between them and could not account for the superconductivity. Both samples showed up to 50% oxygen vacancies in the CuO_2 planes as in Sr_2CuO_3 , rather than in the SrO layers. Transmission electron microscopy (TEM) measurements^{27,37} confirmed the presence of the oxygen vacancies in the CuO_2 planes. The tetragonal structure of $\text{Sr}_2\text{CuO}_{3+\delta}$ thus evidently arises from a random distribution of O vacancies in the CuO_2 square lattice planes, rather than the ordered arrangement of oxygen vacancies in the CuO_2 planes as in orthorhombic Sr_2CuO_3 .

Due to the very large antiferromagnetic Cu–Cu exchange coupling J in Sr_2CuO_3 , the magnitude of the magnetic susceptibility is so low that even small amounts of paramagnetic impurities contribute significantly to the observed magnetic susceptibility. Polycrystalline samples made by Ami *et al.* (Ref. 9) which were exposed to air showed significant Curie-Weiss contributions, observable most easily at low temperatures, which obscured the intrinsic spin susceptibility. The paramagnetic impurity concentrations in the samples responsible for this behavior were small, equivalent to the contribution of 0.4% spins- $\frac{1}{2}$ (with respect to Cu) with g -factor $g = 2$. The impurity concentration decreased dramatically to $\approx 0.1\%$ when the samples were annealed at 600–800 °C in nitrogen or at 300–600 °C in low-pressure (6 torr) helium. It was proposed that paramagnetic oxygen defects due to the uptake of oxygen from the air may be responsible for the Curie-Weiss impurity contribution, but no test of this proposal was carried out. Mitchell *et al.* and Kato *et al.* (Refs. 33, 34) synthesized samples of Sr_2CuO_3 by dehydration of $\text{Sr}_2\text{Cu}(\text{OH})_6$. $\text{Sr}_2\text{Cu}(\text{OH})_6$ loses two molecules of H_2O per formula unit upon heating to 400 °C in an argon atmosphere and forms orthorhombic Sr_2CuO_3 . When heated to ~ 450 °C in oxygen, however, the insulating tetragonal form of $\text{Sr}_2\text{CuO}_{3+\delta}$ discussed above is formed.

In view of the importance of Sr_2CuO_3 as a model $S = \frac{1}{2}$ antiferromagnetic Heisenberg chain compound, it is important to understand the dependence of sample handling on the magnetic properties of Sr_2CuO_3 . We therefore undertook a study of the chemistry associated with sample handling. We found that Sr_2CuO_3 decomposes in air to form $\text{Sr}_2\text{Cu}(\text{OH})_6$, $\text{Sr}(\text{OH})_2$, $\text{Cu}(\text{OH})_2$ and SrCO_3 . $\text{Sr}_2\text{Cu}(\text{OH})_6$ is the main product in this reversible reaction. Direct exposure of Sr_2CuO_3 to liquid water results in immediate irreversible decomposition to $\text{Sr}_2\text{Cu}(\text{OH})_6$ which then further decomposes to SrCO_3 and $\text{Cu}(\text{OH})_2$. Following Sec. II which gives experimen-

tal details of our work, these chemical reactions will be discussed in Sec. III.

In Sec. IV we discuss the crystallography of $\text{Sr}_2\text{Cu}(\text{OH})_6$ which we synthesized in pure form. In Sec. V we present and analyze our isothermal magnetization versus magnetic field $M(H)$ and magnetic susceptibility χ versus temperature T data for $\text{Sr}_2\text{Cu}(\text{OH})_6$. We also report in this section the results of room-temperature electron paramagnetic resonance (EPR) measurements. Our results and conclusions are summarized in Sec. VI. Anticipating that section, we demonstrate that $\text{Sr}_2\text{Cu}(\text{OH})_6$ contains weakly interacting Cu^{+2} magnetic moments with spin $S = \frac{1}{2}$ and average g factor 2.133. From a fit of $\chi(T)$ by the Curie-Weiss law and the $M(H)$ isotherms by modified Brillouin functions, the exchange interaction between adjacent Cu^{+2} spins was found to be $J/k_B = -1.06(4)$ K, a weakly antiferromagnetic interaction.

II. EXPERIMENTAL DETAILS

Several samples of Sr_2CuO_3 were synthesized by calcining stoichiometric quantities of 99.995% pure (metals basis) SrCO_3 (Aithaca Chemical Corp.) and CuO (Alfa Aesar) in air at 950 °C for several days, regrinding once per day. A powder x-ray diffraction (XRD) pattern taken on a Rigaku x-ray diffractometer with $\text{CuK}\alpha$ radiation is shown as the top trace in Fig. 1. A typical sample showed the reported orthorhombic structure, with lattice parameters $a = 12.72(4)$ Å, $b = 3.904(8)$ Å, and $c = 3.496(8)$ Å in good agreement with literature values.^{8,9} XRD also revealed trace amounts of the SrCO_3 and CuO starting materials in the samples as shown in the top-most x-ray pattern in Fig. 1.

Samples of $\text{Sr}_2\text{Cu}(\text{OH})_6$ were characterized by XRD analysis using the above diffractometer. Samples were mixed with dry KBr and pelletized for mid-range infrared spectroscopy (IR) measurements on a Hartmann and Braun Bomem FT-IR. Room-temperature EPR measurements were carried out at 9.5 GHz on a Bruker instrument. The derivative spectrum, dI/dB , shown in Fig. 6 below was obtained in the usual way as a function of magnetic field, but is plotted as a function of the spectroscopic splitting factor (g -factor) g to provide direct comparison with the spectrum reported in the literature.^{38,39} Magnetic susceptibility and magnetization measurements below 300 K were carried out using a Quantum Design superconducting quantum interference device (SQUID) magnetometer. The contribution of ferromagnetic impurities to the measured magnetization was determined from magnetization versus magnetic field isotherms between 75 and 300 K and was found to be equivalent to that of ~ 50 ppm ferromagnetic iron metal impurities; this contribution is corrected for in Figs. 7 and 8 below.

III. DECOMPOSITION OF Sr_2CuO_3

We initially suspected that Sr_2CuO_3 reacts with air when we observed that pristine dark brown Sr_2CuO_3 changes color to blue-gray within about thirty minutes of exposure to air. The subsequent XRD pattern contained the expected Sr_2CuO_3 peaks, but also contained several impurity peaks which could not be identified with remnants of the SrCO_3 or CuO starting materials. The above process was repeated with additional samples to confirm the results. We found that the time required for the above color change to occur ranged up to several days, depending on the relative humidity of the laboratory air, which suggested that the samples were reacting with the water vapor in the air. Degraded samples which were heated to 950°C in air exhibited XRD patterns identical to the XRD pattern of a freshly prepared Sr_2CuO_3 sample (those x-rays were taken with the sample in flowing helium gas to prevent sample degradation while the x-ray data were accumulated). Therefore we conclude that the degradation of Sr_2CuO_3 in air is reversible. Although not the primary focus of this paper, we describe below some preliminary experiments carried out to investigate the observed sample degradation.

Since the time scale for sample degradation was clearly humidity dependent, for controlled experiments a humidity chamber was constructed in which a flow of hydrated 98% pure nitrogen or oxygen gas was passed over a Sr_2CuO_3 sample. The gas was hydrated by diffusing it through deionized water. The relative humidity and temperature inside the chamber were measured with a Fisher Scientific Jumbo Thermo-Humidity Meter. For sample exposure times up to forty-five hours, the sample decomposition results in both gases were identical. Figure 1 shows the progression of the x-ray diffraction patterns versus time for a Sr_2CuO_3 sample exposed to hydrated oxygen gas. The relative humidity of the chamber increased from 50% to 80% and the temperature ranged from 18.7 to 20.4°C over the forty-two hour period in Fig. 1. The sample decomposed primarily into $\text{Sr}_2\text{Cu}(\text{OH})_6$, but small amounts of $\text{Cu}(\text{OH})_2$, $\text{Sr}(\text{OH})_2$ and SrCO_3 could also be identified from XRD patterns as shown in Fig. 1. The amount of SrCO_3 greatly increased when samples were left in the chamber for longer periods which we attribute to reaction of the sample with the impurity CO_2 present in the flowing gas.

Sr_2CuO_3 was next reacted directly with deionized liquid water in air and a sky-blue precipitate immediately formed. Solutions were stirred for several minutes to ensure complete reaction. During this time the precipitate changed to a mixture of black particles and white particles. The precipitate was allowed to settle and then the solution was filtered. XRD analysis of the precipitate showed that it was a mixture of $\text{Cu}(\text{OH})_2$ and SrCO_3 . After heating the mixed precipitate overnight at 125°C , XRD analysis revealed that the SrCO_3 was unchanged but that the $\text{Cu}(\text{OH})_2$ had converted to CuO . The filtrate solution was kept in a sealed jar for observation.

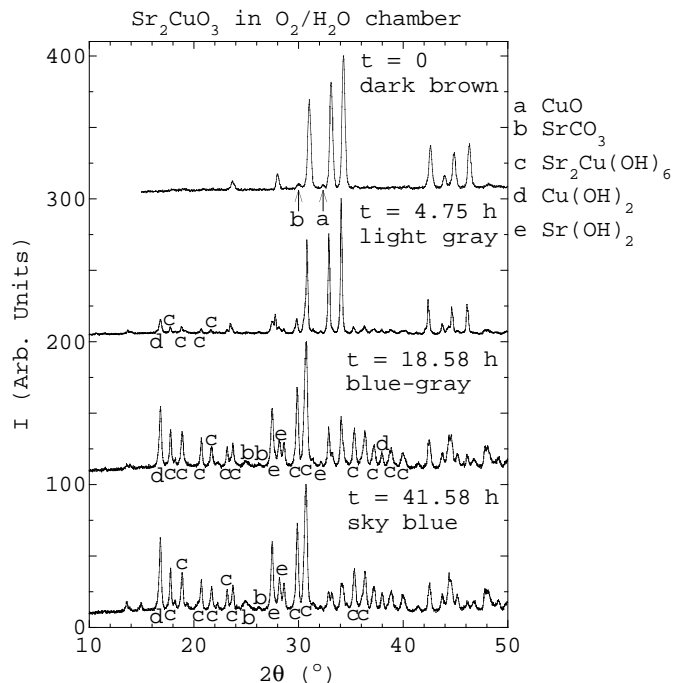


FIG. 1: Successive x-ray diffraction patterns ($\text{CuK}\alpha$ radiation) showing the decomposition of a Sr_2CuO_3 sample with time during exposure to flowing hydrated O_2 gas. The solid curves are the diffracted x-ray intensity I versus diffraction angle 2θ and the letters mark the reflections of different impurity phases according to the legend. The top trace is the initial Sr_2CuO_3 pattern which shows the presence of small amounts of the SrCO_3 and CuO starting materials. Each x-ray diffraction pattern is scaled so that the most intense reflection has an intensity of 100.

A substantial amount of white solid appeared in the solution three to four days later which was identified as SrCO_3 through XRD analysis. We attribute the formation of SrCO_3 to the reaction of unprecipitated Sr^{+2} ions with CO_3^{-2} ions and/or dissolved CO_2 gas present in the water.

In order to isolate the primary decomposition product $\text{Sr}_2\text{Cu}(\text{OH})_6$ and minimize formation of SrCO_3 , exposure of the sample to CO_2 must be minimized. Therefore reaction of a Sr_2CuO_3 sample in a vacuum-tight vessel with nanopure deionized, degassed water was carried out. Two methods of removing gases from the water were used: (i) distillation and (ii) repeated sequences of freezing the water from the bottom up in a vacuum-sealed glass vessel followed by pumping on the water while melting the ice. Initially all samples formed blue or purple-blue precipitates. The purple samples may have contained $\text{SrCu}(\text{OH})_4$ which is a violet-colored sister compound to $\text{Sr}_2\text{Cu}(\text{OH})_6$ (see Refs. 40, 41). We were not able to confirm the presence of $\text{SrCu}(\text{OH})_4$ because all of the precipitates changed color before they could be isolated. Samples were dried by decanting off as much water as possible, then pumping off the residual water.

TABLE I: Summary of reactions of Sr_2CuO_3 with nanopure deionized, degassed water in a vacuum-tight vessel. “Initial color” refers to the color of the solid which immediately formed when the Sr_2CuO_3 sample contacted the water. “Final color” refers to the color of the solid after it had been dried.

| METHOD OF DEGASSING WATER | INITIAL COLOR | FINAL COLOR |
|--------------------------------------|---------------|------------------------|
| freeze/thaw | blue-purple | pale blue ^a |
| freeze/thaw | pale blue | pale blue-green |
| distilled in N_2 atmosphere | purple | blue-green |
| distilled in N_2 atmosphere | dark blue | green |
| distilled in N_2 atmosphere | sky blue | green ^b |

^aX-ray had primarily $\text{Sr}_2\text{Cu}(\text{OH})_6$ peaks.

^bTurned to this color before vacuum pumping began.

They were not exposed to the air. All samples except one turned color from purple-blue to a shade of green during the drying process. The XRD patterns of the green samples (not shown or further discussed here) were complex and the phases present in the green samples could not be identified. The purple-blue sample that did not change color during the drying process was identified as primarily $\text{Sr}_2\text{Cu}(\text{OH})_6$ by XRD analysis. The method of degassing the water did not seem to affect the overall results of the above experiments which are summarized in Table I.

IV. CHARACTERIZATION AND CRYSTAL STRUCTURE OF $\text{Sr}_2\text{Cu}(\text{OH})_6$

In order to characterize the properties of pure $\text{Sr}_2\text{Cu}(\text{OH})_6$, a pure sample of this compound was synthesized in strong hydroxide solution following the method of Scholder *et al.* (Ref. 40) using 99.2% $\text{Cu}(\text{NO}_3)_2 \cdot 2\frac{1}{2}\text{H}_2\text{O}$ (Fisher Scientific) and 99% $\text{Sr}(\text{OH})_2 \cdot 8\text{H}_2\text{O}$ (Alfa Aesar). Figure 2 shows an IR scan of the $\text{Sr}_2\text{Cu}(\text{OH})_6$ sample. The scan shows no evidence of the sister compound $\text{SrCu}(\text{OH})_4$ and agrees with literature data.⁴¹ Inductively coupled plasma (ICP) analysis revealed a Sr:Cu atomic ratio of 2.195 ± 0.066 .

Figure 3 shows the crystal structure of $\text{Sr}_2\text{Cu}(\text{OH})_6$ based on structural data from Nadezhina *et al.*^{42,43} This figure emphasizes the highly elongated Jahn-Teller distorted $\text{Cu}(\text{OH})_6$ octahedra. The equatorial Cu-O distances are 1.97 and 1.98 Å and the apical distance is 2.63 Å. The latter distance is so large that the Cu coordination by oxygen should probably be considered to be square planar rather than octahedral. The $\text{Cu}(\text{OH})_6$ units are isolated from one another suggesting a weak exchange interaction between the Cu^{+2} spins $\frac{1}{2}$. Figure 4 shows an x-ray diffraction pattern of a typical sample which we indexed on a monoclinic lattice, with space group $\text{P}2_1/\text{b}$ (# 14) and with lattice parameters $a = 8.080(2)$ Å, $b = 9.760(2)$ Å, $c = 6.146(1)$ Å and $\gamma = 143.64(1)^\circ$ in agreement with the results of Nadezhina *et al.*^{42,43} A structure study by Dubler *et al.* (Refs. 44, 45)

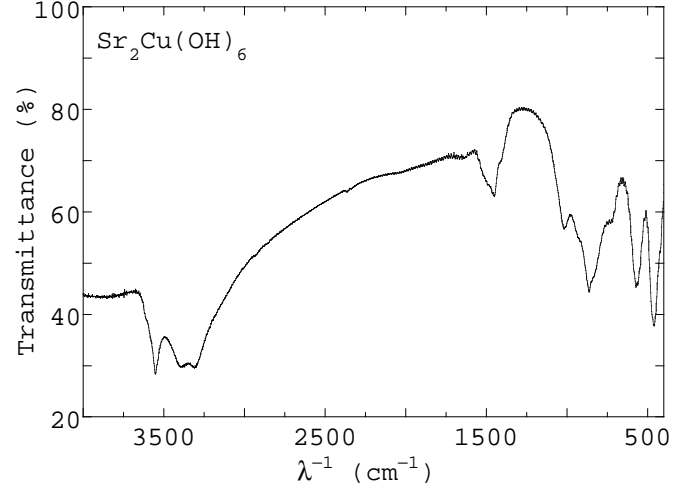


FIG. 2: Mid-range infrared spectroscopy spectrum showing transmittance versus wavenumber (λ^{-1}) for $\text{Sr}_2\text{Cu}(\text{OH})_6$.

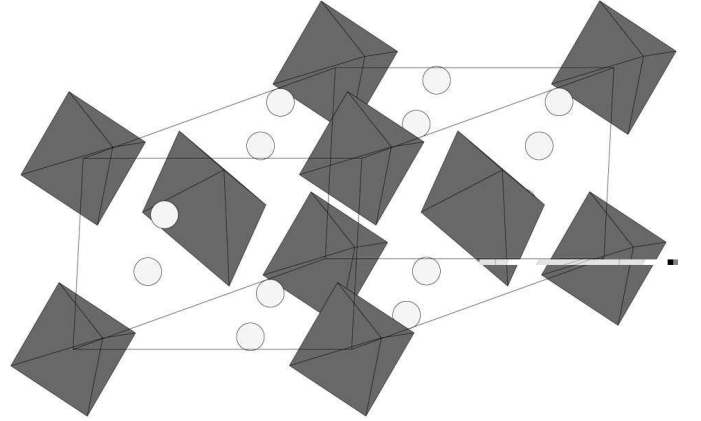


FIG. 3: Crystal structure of $\text{Sr}_2\text{Cu}(\text{OH})_6$. The gray octahedra are $\text{Cu}(\text{OH})_6$ units and the spheres represent Sr^{+2} ions.

reported a different unit cell with different atomic positions in the same space group for $\text{Ba}_2\text{Cu}(\text{OH})_6$. In order to confirm Dubler *et al.*’s statement that $\text{Ba}_2\text{Cu}(\text{OH})_6$ is isostructural to $\text{Sr}_2\text{Cu}(\text{OH})_6$, we undertook a study of the relationships of the two respective unit cells and atomic positions after first correcting for the different space group settings used by the two groups. Figure 5 shows the geometrical relationship between the two unit cells and Table II lists the respective lattice parameters.

The two unit cells coincide in the \hat{z} (c) direction, but form different parallelograms in the ab plane. The a lattice parameter in Nadezhina *et al.*’s unit cell (black cell in the foreground of Fig. 5) is the short diagonal of the parallelogram formed by Dubler *et al.*’s unit cell (gray cell in the background of Fig. 5). The law of cosines was used to obtain the expressions

$$a = \sqrt{a'^2 + b'^2 + 2a'b' \cos \gamma'}$$

TABLE II: Lattice parameters for $\text{Ba}_2\text{Cu}(\text{OH})_6$ by Dubler *et al.* (Refs. 44, 45) and $\text{Sr}_2\text{Cu}(\text{OH})_6$ by Nadezhina *et al.* (Refs. 42, 43). The $\text{Ba}_2\text{Cu}(\text{OH})_6$ primed lattice parameters are listed by Dubler in a different space group setting. The unprimed lattice parameters correspond to the alternate unit cell used by Nadezhina. The relationship between the two unit cells is shown in Fig. 5.

| $\text{Ba}_2\text{Cu}(\text{OH})_6$ Primed | | $\text{Ba}_2\text{Cu}(\text{OH})_6$ Unprimed | | $\text{Sr}_2\text{Cu}(\text{OH})_6$ | |
|--|-------------------------|--|-------------------------|-------------------------------------|-------------------------|
| a' | 6.030(2) Å | a | 8.391(1) Å | a | 8.079(2) Å |
| b' | 10.115(2) Å | b | 10.115(2) Å | b | 9.759(2) Å |
| c' | 6.440(2) Å | c | 6.440(2) Å | c | 6.165(2) Å |
| γ' | 124.03(1)° | γ | 143.44(2)° | γ | 143.620(1)° |
| vol | 325.5(3) Å ³ | vol | 325.6(4) Å ³ | vol | 288.3(2) Å ³ |

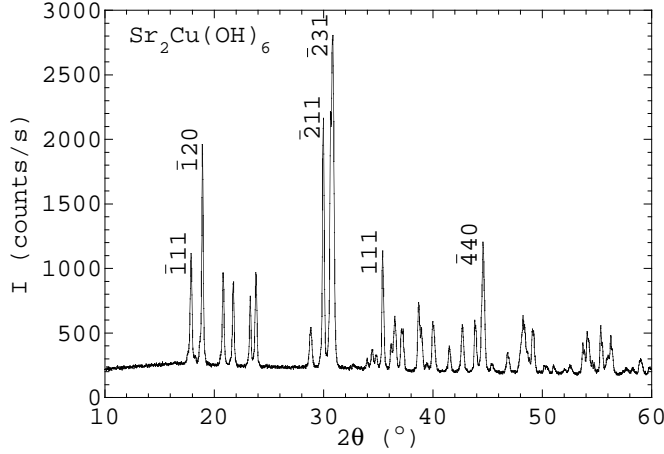


FIG. 4: $\text{CuK}\alpha$ x-ray powder diffraction pattern of $\text{Sr}_2\text{Cu}(\text{OH})_6$. The solid curve is intensity I versus diffraction angle 2θ . The space group is monoclinic $\text{P}2_1/\text{b}$ (14) with $a = 8.080(2)$ Å, $b = 9.760(2)$ Å, $c = 6.146(1)$ Å and $\gamma = 143.64(1)^\circ$. The Miller indices of the six strongest reflections are as indicated.

$$\begin{aligned} b &= b' \\ c &= c' \end{aligned} \quad (1)$$

$$\gamma = 180^\circ - \gamma' + \theta$$

$$\theta = \cos^{-1} \left(\frac{b'^2 - a^2 - a'^2}{-2aa'} \right)$$

which were used to calculate the unprimed unit cell for $\text{Ba}_2\text{Cu}(\text{OH})_6$ which corresponds to Nadezhina *et al.*'s unit cell for $\text{Sr}_2\text{Cu}(\text{OH})_6$. The volumes of the unit cells are $325.6(4)$ Å³ for $\text{Ba}_2\text{Cu}(\text{OH})_6$ and $288.3(2)$ Å³ for $\text{Sr}_2\text{Cu}(\text{OH})_6$, a difference of $37.3(6)$ Å³. This difference is similar to four times the difference between the Ba and Sr atomic volumes calculated from structural data for elemental Ba and Sr (Ref. 46): $4(62.99 \text{ Å}^3/\text{atom} - 56.325 \text{ Å}^3/\text{atom}) = 26.66 \text{ Å}^3/\text{atom}$ (the factor of 4 arises

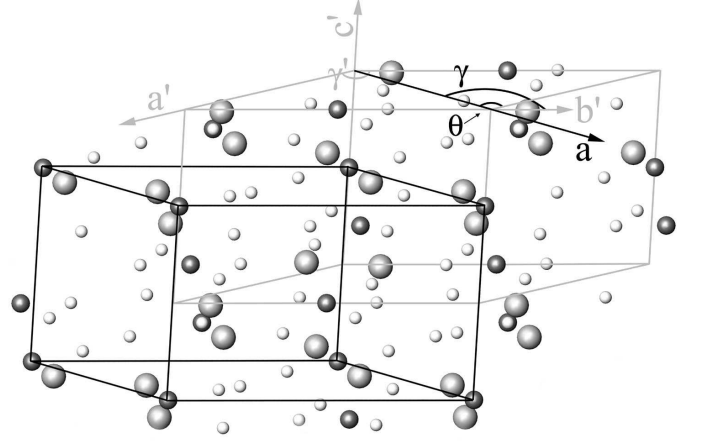


FIG. 5: Two alternative unit cells for $(\text{Ba,Sr})_2\text{Cu}(\text{OH})_6$. Dubler *et al.* (Refs. 44, 45) used the gray cell in the background with the primed lattice parameters for $\text{Ba}_2\text{Cu}(\text{OH})_6$. The black cell in the foreground is an alternate choice and corresponds to the unit cell used by Nadezhina *et al.* (Refs. 42, 43) for $\text{Sr}_2\text{Cu}(\text{OH})_6$. a is the short diagonal of the $a'b'$ parallelogram, b and c are equivalent to b' and c' , respectively, and γ is the angle between a and b . θ is the angle between a and a' . Note that the black cell is shifted in the c direction so that Cu^{+2} ions are on the corners. Small spheres represent O^{2-} , medium spheres Cu^{+2} and large spheres Ba^{+2} ions. (Courtesy of Julia K. Burzon)

because there are two formula units per unit cell). Also, since in the same (unprimed) unit cell the γ angles of the unit cells for the two compounds are essentially the same and the a , b , and c lattice parameters for the Ba compound are all $\sim 4\%$ larger than those for the Sr compound, one sees that substituting Ba for Sr results in a uniform increase in unit cell size.

The fractional atomic positions in the primed unit cell for $\text{Ba}_2\text{Cu}(\text{OH})_6$ can be expressed in terms of the unprimed unit cell according to

$$\begin{pmatrix} x/a \\ y/b \\ z/c \end{pmatrix} = - \left[\begin{pmatrix} -\frac{a' \sin \gamma'}{a \sin \gamma} & 0 & 0 \\ \frac{a' \sin(\gamma' + \gamma)}{b \sin \gamma} & \frac{b'}{b} & 0 \\ 0 & 0 & \frac{c'}{c} \end{pmatrix} \begin{pmatrix} x'/a' \\ y'/b' \\ z'/c' \end{pmatrix} - \begin{pmatrix} 0 \\ 0 \\ \frac{1}{2} \end{pmatrix} \right]. \quad (2)$$

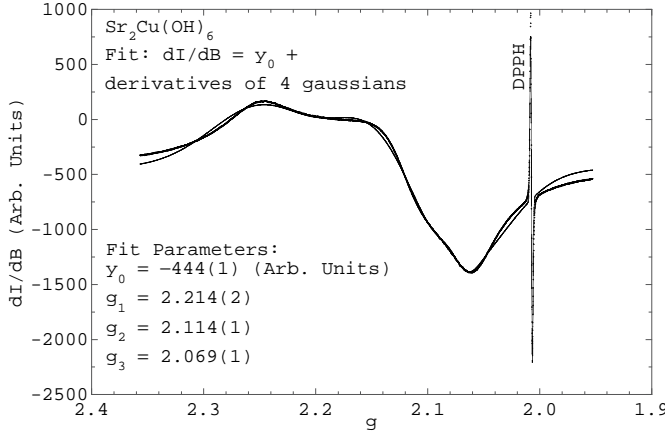


FIG. 6: The thick curve is a powder EPR derivative spectrum, dI/dB versus spectroscopic splitting factor g of $\text{Sr}_2\text{Cu}(\text{OH})_6$ at room temperature using an rf frequency of 9.5 GHz (X-band). The thin curve is a multiple gaussian derivative fit to the data with parameters shown in the figure. DPPH ($g = 2.0036$) was used as an internal magnetic field standard.

The results are shown in Table III. Although the unprimed atomic positions for $\text{Ba}_2\text{Cu}(\text{OH})_6$ do not match those of $\text{Sr}_2\text{Cu}(\text{OH})_6$ within the errors, the close similarities of the respective values demonstrate that $\text{Sr}_2\text{Cu}(\text{OH})_6$ and $\text{Ba}_2\text{Cu}(\text{OH})_6$ are isostructural. Therefore, the primed unit cell used by Dubler *et al.* is an alternative unit cell for the two compounds.

V. EPR, MAGNETIC SUSCEPTIBILITY, AND MAGNETIZATION OF $\text{Sr}_2\text{Cu}(\text{OH})_6$

Figure 6 shows a typical room-temperature EPR spectrum of a powder $\text{Sr}_2\text{Cu}(\text{OH})_6$ sample and a DPPH internal standard. The hyperfine interaction of the Cu^{+2} electronic spin- $\frac{1}{2}$ with the Cu nuclear spin $I = \frac{3}{2}$ has a typical width of 20–100 G,⁴⁷ but it is not resolved in our data. We believe this is due to several factors. We expect to see “absorption-like” features rather than sharp derivative peaks since the material is a powder.⁴⁸ At room temperature, spin-lattice relaxation leads to broadened features which obscure the hyperfine peaks.^{49,50} Since our system is not magnetically dilute, the spin-spin interaction also leads to peak broadening.⁵⁰

The function used to fit the EPR data consisted of a vertical offset term and the sum of the derivatives of four gaussians (including one for the DPPH magnetic field marker) which yielded three principal-axis g values for $\text{Sr}_2\text{Cu}(\text{OH})_6$ consistent with the rhombic symmetry of the Cu site. The DPPH-corrected g values, 2.214(2), 2.114(1), and 2.069(1), are in agreement with the literature values.^{38,39} In order to incorporate these experimentally determined values into fits to the powder magnetic susceptibility and magnetization data, the spherical (powder) average must be used. The Curie constant

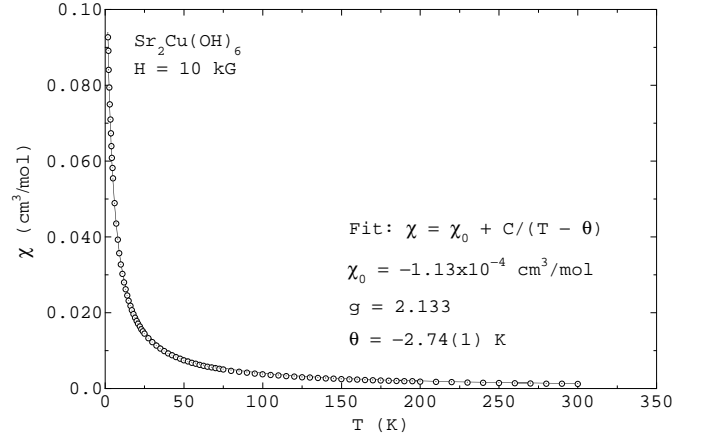


FIG. 7: Magnetic susceptibility χ versus temperature T of $\text{Sr}_2\text{Cu}(\text{OH})_6$ (\odot). The solid curve is a fit to the data by the function shown in the figure [Eq. (5)], with parameters also listed in the figure where g is g_A as given in Eq. (3).

which occurs in the magnetic susceptibility fit function [Eqs. (5, 6, 8) below] is a function of g^2 ; therefore, the appropriate average of g is the rms g value, g_A , as given in Eq. (3). The Brillouin function [Eq. (10) below] used to fit our low temperature magnetization data is a function of the average of g itself, as given by g_B in Eq. (4). Not surprisingly, these two values are nearly identical.

$$g_A = \sqrt{\frac{(g_1^2 + g_2^2 + g_3^2)}{3}} = 2.133 \quad (3)$$

$$g_B = \frac{(g_1 + g_2 + g_3)}{3} = 2.132 \quad (4)$$

The magnetic susceptibility χ versus temperature T in an applied magnetic field $H = 10 \text{ kG}$ is shown in Fig. 7. We fitted the data by

$$\chi = \chi_0 + \frac{C}{T - \theta}, \quad (5)$$

where θ is the Weiss temperature and C is the Curie constant given by

$$C = \frac{Ng^2\mu_B^2S(S+1)}{3k_B} \quad (6)$$

in which N is the number of spins in the sample, g is g_A (Eq. (3)), μ_B is the Bohr magneton, S is the spin of the Cu^{+2} ion (assumed to be $\frac{1}{2}$) and k_B is the Boltzmann constant. In the molar units of χ or M in Figs. 7, 8, 10, and 11 below, N is set to N_A (Avogadro's number). The T -independent χ_0 term

$$\chi_0 = \chi^{\text{core}} + \chi^{\text{VV}} \quad (7)$$

is the sum of the contribution from the diamagnetic cores of the atoms χ^{core} plus the paramagnetic Van Vleck susceptibility χ^{VV} of the Cu^{+2} ions.

TABLE III: Atomic positions for $\text{Ba}_2\text{Cu}(\text{OH})_6$ by Dubler *et al.* (Refs. 44, 45, primed unit cell) and $\text{Sr}_2\text{Cu}(\text{OH})_6$ by Nadezhina *et al.* (Refs. 42, 43, unprimed unit cell). The ‘primed’ atomic positions for $\text{Ba}_2\text{Cu}(\text{OH})_6$ correspond to the ‘primed’ unit cell in Table II. The ‘unprimed’ atomic positions for $\text{Ba}_2\text{Cu}(\text{OH})_6$ are obtained by expressing the primed positions in terms of the unprimed unit cell listed in Table II [see Eq. (2)]. These unprimed positions are similar to those obtained by Nadezhina *et al.* for $\text{Sr}_2\text{Cu}(\text{OH})_6$.

| | $\text{Ba}_2\text{Cu}(\text{OH})_6$ Primed | | | $\text{Ba}_2\text{Cu}(\text{OH})_6$ Unprimed | | | $\text{Sr}_2\text{Cu}(\text{OH})_6$ | | |
|--------|--|---------------|-----------|--|---------------|---------------|-------------------------------------|---------------|---------------|
| | x'/a' | y'/b' | z'/c' | x/a | y/b | z/c | x/a | y/b | z/c |
| Ba, Sr | 0.2821(1) | 0.0674(1) | 0.2489(1) | 0.2820(4) | 0.0332(5) | 0.4326(1) | 0.2866(2) | 0.0367(2) | 0.4256(2) |
| Cu | 0 | $\frac{1}{2}$ | 0 | 0 | $\frac{1}{2}$ | $\frac{1}{2}$ | 0 | $\frac{1}{2}$ | $\frac{1}{2}$ |
| O1 | 0.4327(8) | 0.2575(6) | 0.0586(4) | 0.4326(13) | 0.3740(17) | 0.2425(8) | 0.429(2) | 0.366(2) | 0.233(2) |
| O2 | 0.1956(8) | 0.7629(5) | 0.0393(4) | 0.1956(10) | 0.1563(14) | 0.7371(10) | 0.202(2) | 0.156(2) | 0.724(2) |
| O3 | 0.1387(8) | 0.4750(6) | 0.2267(4) | 0.1387(9) | 0.9120(14) | 0.0250(9) | 0.122(2) | 0.889(2) | 0.033(2) |

A fit to all the $\chi(T)$ data in Fig. 7 by Eq. (5) with χ_0 set to the diamagnetic core contribution for $\text{Sr}_2\text{Cu}(\text{OH})_6$ ($-1.13 \times 10^{-4} \text{ cm}^3/\text{mol}$), yields the fit (solid curve) in Fig. 7 with a Weiss temperature $\theta = -2.74(1) \text{ K}$ indicating weak coupling between the Cu^{+2} spins- $\frac{1}{2}$, as expected. The negative sign of θ corresponds to an anti-ferromagnetic coupling between the Cu spins. When χ_0 was allowed to vary, χ_0 became more negative than the diamagnetic core contribution, which is physically unreasonable. We were able to obtain a better fit when C was allowed to vary. However, the fitted C value yielded a g value from Eq. (6) which was significantly lower than the measured average g value obtained from EPR.

Figure 8 shows the inverse of the magnetic susceptibility corrected for the contribution of χ_0 , $(\chi - \chi_0)^{-1}$, versus temperature T in an applied magnetic field $H = 10 \text{ kG}$. The dashed line is a linear fit

$$\frac{1}{\chi - \chi_0} = \frac{T - \theta}{C} \quad (8)$$

[see Eq. (5)] with fixed C given by Eq. (6) which yields $\theta = -8.0(5) \text{ K}$. This θ is significantly larger in magnitude than obtained from the $\chi(T)$ fit in Fig. 7. The solid line in Fig. 8 is a linear fit with fitted C and is clearly a better fit to the data. Although the latter $\theta = -2.75(9) \text{ K}$ agrees with that from the fit in Fig. 7, the average $g = 2.074(1)$ obtained from C is lower than the average value obtained from EPR. We could not obtain an optimum fit to our data with physically reasonable parameters using the g value from the EPR measurements. At low temperatures, shown in Fig. 8(b), both the ‘‘Fitted g ’’ and the ‘‘Fixed g ’’ fits deviate from the data.

As noted above, the θ values obtained from the fixed- g fits to $\chi(T)$ and $(\chi - \chi_0)^{-1}$ versus T do not agree. Fitting $\chi(T)$ emphasizes the low-temperature regime where χ is varying most strongly with T due to the Curie-Weiss behavior. The $(\chi - \chi_0)^{-1}$ data, however, emphasize the high-temperature behavior, where weak temperature dependence of χ_0 and/or the contribution to $\chi(T)$ from small amounts of impurities could most strongly influence the parameters obtained from the fit. Therefore, the parameters obtained from the one-parameter $\chi(T)$

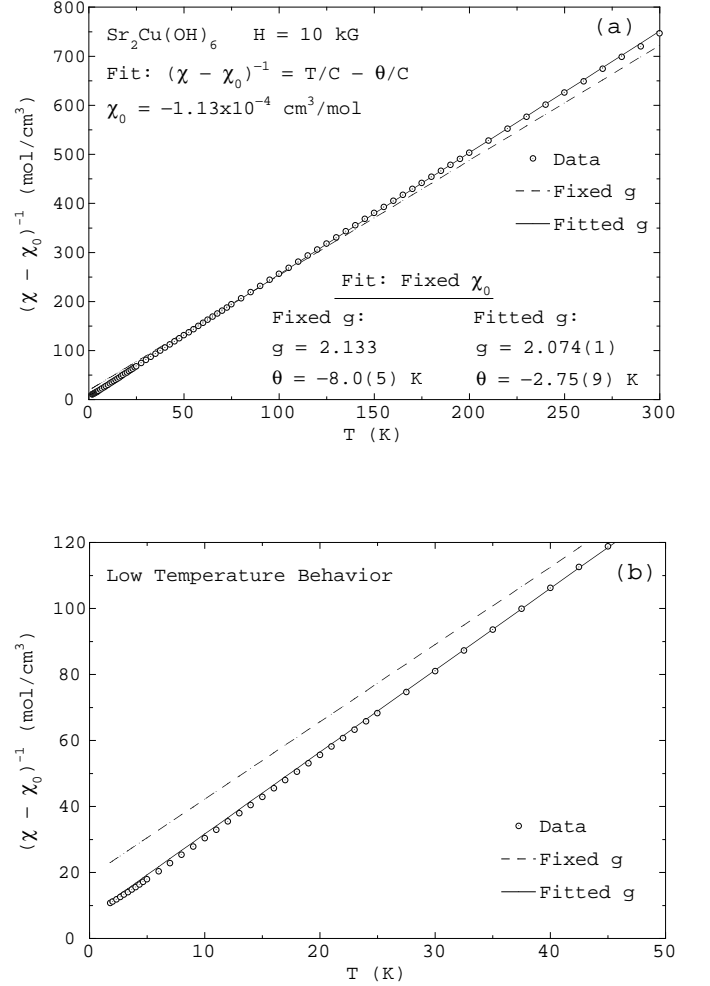


FIG. 8: (a) Inverse magnetic susceptibility corrected for the contribution of χ_0 , $(\chi - \chi_0)^{-1}$, versus temperature T (\odot) of $\text{Sr}_2\text{Cu}(\text{OH})_6$. The dashed line is the ‘‘Fixed g ’’ fit yielding the θ parameter shown in the figure where the fixed g is g_A in Eq. (3). The solid line is the ‘‘Fitted g ’’ fit which yields the indicated g and θ values. χ_0 is fixed at χ^{core} for both fits. (b) Expanded plot of the low temperature data and fits below 50 K.

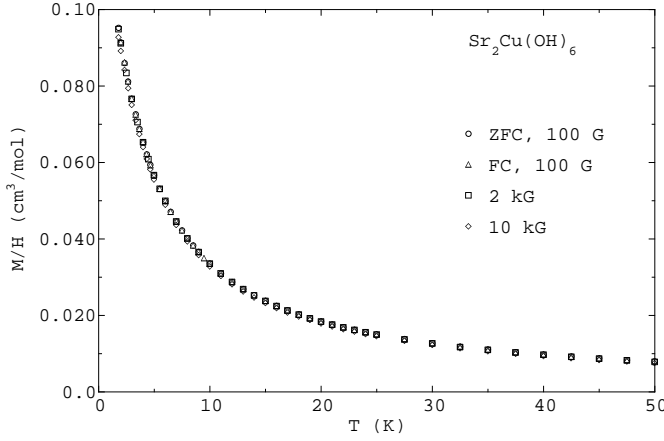


FIG. 9: Magnetization divided by magnetic field M/H versus temperature T for $\text{Sr}_2\text{Cu}(\text{OH})_6$. The zero-field-cooled (ZFC) and field-cooled (FC) data (\circ and \triangle , respectively) were taken in an applied magnetic field of $H = 100$ G. Also shown are data taken in $H = 2$ kG (\square) and 10 kG (\diamond).

fit,

$$\begin{aligned}\chi_0 &= -1.13 \times 10^{-4} \text{ cm}^3/\text{mol} \\ g &= 2.133 \\ \theta &= -2.74(1) \text{ K},\end{aligned}\tag{9}$$

are considered to be more reliable and best represent the intrinsic behavior of $\text{Sr}_2\text{Cu}(\text{OH})_6$.

To investigate the low temperature behavior further, several magnetization versus applied magnetic field $M(H)$ isotherms at low temperatures and both zero-field-cooled (ZFC) and field-cooled (FC) $M(T)$ data at $H = 100$ G were taken. The ZFC and FC data show no evidence of long-range ordering above 1.8 K as shown in Fig. 9. The $M(H)$ isotherms at low temperatures are shown in Fig. 10. The data up to $H = 1$ T are in the low-field proportional part of the $M(H)$ curves, which explains why all the magnetization data in Fig. 9 lie on a common curve.

We obtained a robust fit to the $M(H)$ isotherm data in Fig. 10 using a modified Brillouin function⁵¹ for $S = \frac{1}{2}$

$$M = NgS \tanh \left[\frac{gS\mu_B H}{k_B(T - \theta)} \right], \tag{10}$$

where g is g_B as given in Eq. (4), and T in the usual Brillouin function⁵¹ is replaced by $T - \theta$. This change was necessary so that the high-temperature and/or low-field expansion of Eq. (10) yielded the observed Curie-Weiss behavior $M = CH/(T - \theta)$. The fit yielded $\theta = -2.575(4)$ K. This value for θ agrees with the value in Eq. (9) obtained from the fit to the magnetic susceptibility data, as it should. A comparison of the two values

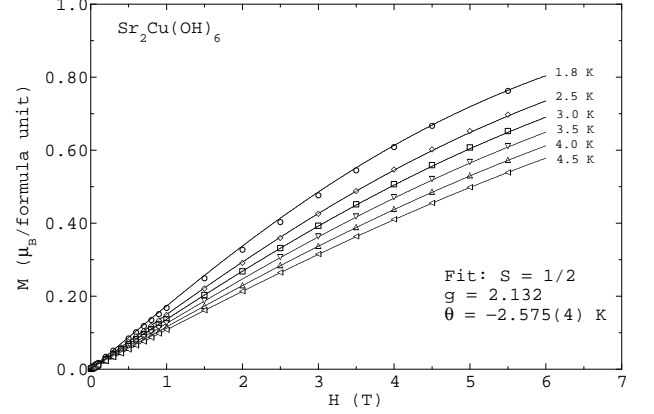


FIG. 10: Magnetization M versus field H for $\text{Sr}_2\text{Cu}(\text{OH})_6$ at 1.8 K (\circ), 2.5 K (\diamond), 3.0 K (\square), 3.5 K (∇), 4.0 K (\triangle) and 4.5 K (\triangleleft). The solid curves are a fit to the data using Eq. (10) with parameters shown in the figure where g is g_B as given in Eq. (4).

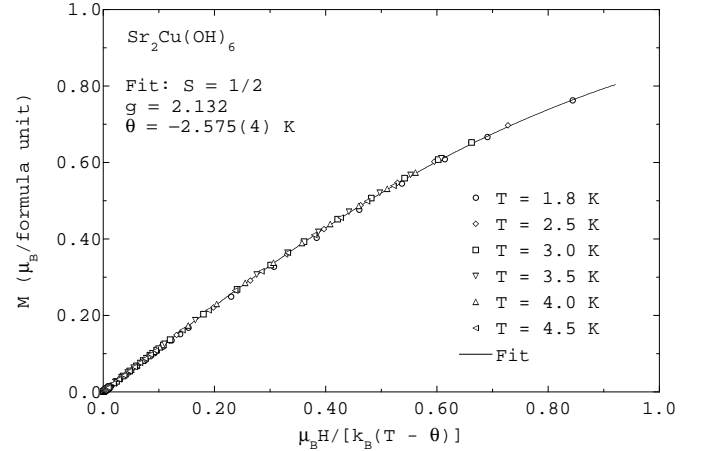


FIG. 11: Magnetization M versus the ratio of magnetic field energy to the modified thermal energy $\mu_B H / k_B(T - \theta)$ for $\text{Sr}_2\text{Cu}(\text{OH})_6$ at 1.8 K (\circ), 2.5 K (\diamond), 3.0 K (\square), 3.5 K (∇), 4.0 K (\triangle) and 4.5 K (\triangleleft). The solid curve is a fit to all the data by Eq. (10), with fitting parameter θ , fixed $g = g_B$ as given in Eq. (4) and $S = 1/2$.

gives the estimate $\theta = -2.66(9)$ K. When we allowed the spin S to vary during a fit, the fitted S value ranged from 0.471 to 0.516 indicating that the spin is indeed $\frac{1}{2}$ as expected for Cu^{+2} . Allowing g to vary at fixed $S = \frac{1}{2}$ produced a slightly better fit, but with an incorrect g value ($g = 2.179$ compared to the actual value 2.132). In Fig. 11, a scaling plot of the magnetization M versus the ratio of magnetic field energy to the modified thermal energy $\mu_B H / k_B(T - \theta)$ is shown and we see that the fit (solid curve) does indeed reproduce the data very well.

In summary, we find that the best description of the

combined EPR, $\chi(T)$ and $M(H)$ data for $\text{Sr}_2\text{Cu}(\text{OH})_6$ is that the Cu^{+2} ions have spin $S = \frac{1}{2}$ with $g = 2.133$; the Weiss temperature in the Curie-Weiss law is $\theta = -2.66(9)$ K. Assuming a Heisenberg interaction between nearest-neighbor spins with Hamiltonian $\mathcal{H} = -J \sum_{\langle i j \rangle} \vec{S}_i \cdot \vec{S}_j$, where the sum is over all distinct nearest-neighbor pairs of spins and $J > 0$ ($J < 0$) corresponds to a ferromagnetic (antiferromagnetic) interaction, the exchange constant J is given in terms of θ by $J = 3k_B\theta/[zS(S+1)]$ where z is the number of nearest neighbors.⁵¹ In $\text{Sr}_2\text{Cu}(\text{OH})_6$, each Cu atom has 10 Cu nearest neighbors ($z = 10$) at a distance of 5.8–6.2 Å; the Cu next-nearest neighbors are at distances of ≥ 8.1 Å. Using $\theta = -2.66(9)$ K, one thus obtains $J/k_B = -1.06(4)$ K.

VI. SUMMARY AND CONCLUSIONS

We have demonstrated that Sr_2CuO_3 decomposes in both air and liquid water and that the primary decomposition product is $\text{Sr}_2\text{Cu}(\text{OH})_6$. In contrast, the compound La_2CuO_4 can be successfully electrochemically oxidized in aqueous base without any noticeable decomposition.⁵²

The magnetic susceptibility of $\text{Sr}_2\text{Cu}(\text{OH})_6$ exhibits Curie-Weiss behavior down to low temperatures and indicates only very weak interactions between the Cu^{+2} spins. The crystallography, EPR, and magnetization measurements are consistent with a nearly isolated, spin $S = \frac{1}{2}$, local moment model for $\text{Sr}_2\text{Cu}(\text{OH})_6$. We obtained unusually good consistency between the $M(H)$ and $\chi(T)$ fits which yielded a small $\theta = -2.66(9)$ K. The spherically averaged g of the Cu^{+2} spins is 2.133 obtained from EPR and is similar to those of other cuprates. For example, g in CuO is 2.125(5); in $\text{La}_2\text{BaCuO}_5$ and in powder $\text{Sr}_{14}\text{Cu}_{24}\text{O}_{41}$ it is 2.103 and 2.14, respectively (from Table V in Ref. 5).

Since the magnitude of the magnetic susceptibility of the linear chain compound Sr_2CuO_3 is small due to the strong antiferromagnetic coupling between the Cu spins, one would expect even a small impurity concentration of $\text{Sr}_2\text{Cu}(\text{OH})_6$ to produce a significant paramagnetic contribution at low temperatures. Although we cannot rule out the possibility that paramagnetic oxygen species are generated upon exposure of Sr_2CuO_3 to air as proposed by Ami *et al.* (Ref. 9), our experiments indicate that the reported variable Curie-Weiss contributions to the magnetic susceptibility of polycrystalline Sr_2CuO_3 were most likely mainly due to varying amounts of $\text{Sr}_2\text{Cu}(\text{OH})_6$ on the sample surfaces due to exposure of the sample to the humidity in the air.

The Cu–Cu exchange coupling $J/k_B = -1.06(4)$ K in $\text{Sr}_2\text{Cu}(\text{OH})_6$ is very weak compared to $J/k_B \sim -1600$ K in the high- T_c cuprate superconductors, due to the isolated square-planar coordination of the Cu^{+2} ions in $\text{Sr}_2\text{Cu}(\text{OH})_6$. The nearest-neighbor Cu–Cu exchange path is Cu–O–O–Cu with a zig-zag geometry and a Cu–Cu distance of 5.8 Å, whereas in the planar high- T_c cuprates the nearest-neighbor distance is 2.80 Å with a strong 180° Cu–O–Cu antiferromagnetic superexchange coupling. Thus $\text{Sr}_2\text{Cu}(\text{OH})_6$ serves as nice reference material for comparison to the magnetic properties of more strongly interacting systems such as the high- T_c cuprates.

Acknowledgments

We thank Joseph Shinar for useful discussions regarding the EPR spectrum and Paul Kögerler for his help with the IR and EPR measurements. Ames Laboratory is operated for the U.S. Department of Energy by Iowa State University under Contract No. W-7405-Eng-82. This work was supported by the Director for Energy Research, Office of Basic Energy Sciences.

¹ H. A. Bethe, Z. Phys. **71**, 205 (1931).

² M. Uehara, T. Nagata, J. Akimitsu, H. Takahashi, N. Môri, and K. Kinoshita, J. Phys. Soc. Jpn. **65**, 2764 (1996).

³ H. Takahashi, N. Môri, T. Nakanishi, T. Nagata, M. Uehara, J. Akimitsu, and K. Kinoshita, Physica B **237-238**, 112 (1997).

⁴ D. C. Johnston, R. K. Kremer, M. Troyer, X. Wang, A. Klümper, S. L. Bud'ko, A. F. Panchula, and P. C. Canfield, Phys. Rev. B **61**, 9558 (2000).

⁵ D. C. Johnston, M. Troyer, S. Miyahara, D. Lidsky, K. Ueda, M. Azuma, Z. Hiroi, M. Takano, M. Isobe, Y. Ueda, M. A. Korotin, V. I. Anisimov, A. V. Mahajan, L. L. Miller, cond-mat/0001147, and cited references.

⁶ D. C. Johnston, T. Saito, M. Azuma, M. Takano, T. Yamauchi, and Y. Ueda, Phys. Rev. B **64**, 134403 (2001), and cited references.

⁷ E. Dagotto and T. M. Rice, Science **271**, 618 (1996).

⁸ C. L. Teske and H. Muller-Büschbaum, Z. Anorg. Allg.

Chem. **371**, 325 (1969).

⁹ T. Ami, M. K. Crawford, R. L. Harlow, Z. R. Wang, D. C. Johnston, Q. Huang, and R. W. Erwin, Phys. Rev. B **51**, 5994 (1995).

¹⁰ D. C. Johnston, Acta Phys. Pol. A **91**, 181 (1997).

¹¹ N. Motoyama, H. Eisaki, and S. Uchida, Phys. Rev. Lett. **76**, 3212 (1996).

¹² S. Eggert, Phys. Rev. B **53**, 5116 (1996).

¹³ H. Suzuura, H. Yasuhara, A. Furusaki, N. Nagaosa, and Y. Tokura, Phys. Rev. Lett. **76**, 2579 (1996).

¹⁴ J. Lorenzana and R. Eder, Phys. Rev. B **55**, R3358 (1997).

¹⁵ S.-L. Drechsler, J. Málek, S. Zališ, and K. Rościszewski, Phys. Rev. B **53**, 11328 (1996).

¹⁶ K. M. Kojima, Y. Fudamoto, M. Larkin, G. M. Luke, J. Merrin, B. Bachumi, Y. J. Uemura, N. Motoyama, H. Eisaki, S. Uchida, et al., Phys. Rev. Lett. **78**, 1787 (1997).

¹⁷ A. Keren, L. P. Le, G. M. Luke, B. J. Sternlieb, W. D.

- Wu, Y. J. Uemura, S. Tajima, and S. Uchida, Phys. Rev. B **48**, 12926 (1993).
- ¹⁸ A. Keren, K. Kojima, L. P. Le, G. M. Luke, W. D. Wu, Y. J. Uemura, S. Tajima, and S. Uchida, J. Magn. Magn. Mater. **140-144**, 1641 (1995).
 - ¹⁹ S. Eggert, I. Affleck, and M. Takahashi, Phys. Rev. Lett. **73**, 332 (1994).
 - ²⁰ A. Klümper and D. C. Johnston, Phys. Rev. Lett. **84**, 4701 (2000).
 - ²¹ M. Takigawa, N. Motoyama, H. Eisaki, and S. Uchida, Phys. Rev. Lett. **76**, 4612 (1996).
 - ²² M. Takigawa, N. Motoyama, H. Eisaki, and S. Uchida, Phys. Rev. B **55**, 14129 (1997).
 - ²³ M. Takigawa, O. A. Starykh, A. W. Sandvik, and R. R. P. Singh, Phys. Rev. B **56**, 13681 (1997).
 - ²⁴ H. Fujisawa, T. Yokoya, T. Takahashi, S. Miyasaka, M. Kibune, and H. Takagi, Phys. Rev. B **59**, 7358 (1999), and cited references.
 - ²⁵ Z. Hiroi, M. Takano, M. Azuma, and Y. Takeda, Nature **364**, 315 (1993).
 - ²⁶ P. D. Han, L. Chang, and D. A. Payne, Physica C **228**, 129 (1994).
 - ²⁷ Y. Y. Wang, H. Zhang, V. P. Dravid, L. D. Marks, P. D. Han, and D. A. Payne, Physica C **255**, 247 (1995).
 - ²⁸ P. Laffez, X. J. Wu, S. Adachi, H. Yamauchi, and N. Môri, Physica C **222**, 303 (1994).
 - ²⁹ T. Ami, M. K. Crawford, R. L. Harlow, Z. G. Li, T. Vogt, Q. Zhu, and D. E. Cox, Physica C **235-240**, 1003 (1994).
 - ³⁰ T. Kawashima, Y. Matsui, and E. Takayama-Muromachi, Physica C **282-287**, 513 (1997).
 - ³¹ T. Kawashima and E. Takayama-Muromachi, Physica C **267**, 106 (1996).
 - ³² R. C. Lobo, F. J. Berry, and C. Greaves, J. Solid State Chem. **88**, 513 (1990).
 - ³³ J. F. Mitchell, D. G. Hinks, and J. L. Wagner, Physica C **227**, 279 (1994).
 - ³⁴ M. Kato, T. Miyajima, I. Nagai, and Y. Koike, J. Low Temp. Phys. **105**, 1499 (1996).
 - ³⁵ M. Bonvalot, E. Beaunon, D. Bourgault, M. N  nez-Regueiro, and R. Tournier, Physica C **282-287**, 539 (1997).
 - ³⁶ Y. Shimakawa, J. D. Jorgensen, J. F. Mitchell, B. A. Hunter, H. Shaked, D. G. Hinks, R. L. Hitterman, Z. Hiroi, and M. Takano, Physica C **228**, 73 (1994).
 - ³⁷ H. Zhang, Y. Y. Wang, L. D. Marks, V. P. Dravid, P. D. Han, and D. A. Payne, Physica C **255**, 257 (1995).
 - ³⁸ C. Friebe, Z. Naturforsch. **29b**, 295 (1974).
 - ³⁹ V. G. Krishnan, Indian J. Pure Appl. Phys. **16**, 794 (1978).
 - ⁴⁰ V. R. Scholder, R. Felsenstein, and A. Apel, Z. Anorg. Allg. Chem. **216**, 138 (1933).
 - ⁴¹ B. N. Ivanov-Emin, L. P. Petrishcheva, B. E. Zaitsev, and A. S. Izmailovich, Zh. Neorg. Khim. **29**, 1497 (1984).
 - ⁴² T. N. Nadezhina, E. A. Pobedinskaya, and N. V. Belov, Sov. Phys. Dok. **25**, 73 (1980).
 - ⁴³ T. N. Nadezhina, E. A. Pobedinskaya, and N. V. Belov, Dokl. Akad. Nauk SSSR **250**, 1126 (1980).
 - ⁴⁴ E. Dubler, P. Korber, and H. R. Oswald, Acta Crystallogr. Sect. B **29**, 1929 (1973).
 - ⁴⁵ E. Dubler, P. Korber, and H. R. Oswald, Naturwissenschaften **59**, 467 (1972).
 - ⁴⁶ W. B. Pearson, *A Handbook of Lattice Spacings and Structures of Metals and Alloys*, vol. 2 (Pergamon Press, New York, 1967).
 - ⁴⁷ J. W. Orton, *Electron Paramagnetic Resonance: An Introduction to Transition Group Ions in Crystals* (Iliffe Books Ltd, London, 1968).
 - ⁴⁸ J. R. Pilbrow, *Transition Ion Electron Paramagnetic Resonance* (Clarendon Press, Oxford, 1990).
 - ⁴⁹ K. D. Bowers and J. Owen, Rep. Prog. Phys. **18**, 304 (1955).
 - ⁵⁰ A. Abragam and B. Bleaney, *Electron Paramagnetic Resonance of Transition Ions* (Clarendon Press, Oxford, 1970).
 - ⁵¹ C. Kittel, *Introduction to Solid State Physics* (John Wiley & Sons, Inc., New York, 1996), 7th ed.
 - ⁵² F. C. Chou and D. C. Johnston, Phys. Rev. B **54**, 572 (1996), and cited references.